Available online at www.sciencedirect.com
SCIENCE DIRECT®
Journal of Power Sources 138 (2004) 1–13
JOURNAL OF POWER SOURCES
www.elsevier.com/locate/jpowsour

Pressure losses in laminar flow through serpentine channels in fuel cell stacks

S. Maharudrayya, S. Jayanti*, A.P. Deshpande

Department of Chemical Engineering, IIT-Madras, Chennai 600036, India

Received 2 April 2004; accepted 9 June 2004
Available online 31 July 2004

Abstract

The pressure losses in the flow distributor plate of the fuel cell depend on the Reynolds number and geometric parameters of the small flow channels. Very little information has been published on the loss coefficients for laminar flow. This study reports a numerical simulation of laminar flow though single sharp and curved bends, 180° bends and serpentine channels of typical fuel cell configurations. The effect of the geometric parameters and Reynolds number on the flow pattern and the pressure loss characteristics is investigated. A three-regime correlation is developed for the excess bend loss coefficient as a function of Reynolds number, aspect ratios, curvature ratios and spacer lengths between the channels. These have been applied to calculate the pressure drop in typical proton-exchange membrane fuel cell configurations to bring out the interplay among the important geometric parameters.
© 2004 Elsevier B.V. All rights reserved.

Keywords: PEM fuel cell; Serpentine channels; Laminar flow; Bend loss coefficients; Computational fluid dynamics; Design correlations

1. Introduction

Fuel cells are electrochemical reactors and are being used for a wide variety of applications. Due to their high efficiency (nearly twice that of the present generation of internal combustion engines), portability and near-zero emissions, fuel cells are attractive as a power source for automobiles. Of the various types of fuel cells, the proton-exchange membrane fuel cell (PEMFC) operates at near-room temperatures and is considered to be a good choice for automotive applications. An elementary PEMFC consist of two thin, porous electrodes (an anode and a cathode), which are separated by a polymer membrane that passes only protons. In order to achieve high utilization of the electrochemically active surfaces, a planar architecture is usually used, in which the reactants, namely hydrogen and oxygen (or their variants) are forced through grooves etched on gas distributor plates. The grooves may be of different patterns, i.e., parallel, single serpentine, parallel serpentine or interdigitated channels [1–4] (Fig. 1). Since the voltage produced across a typical cell is about 1 V, a number of such cells are stacked together and are connected in series to increase the voltage. Cooling of the fuel cells is achieved by inserting a plate between every second or third fuel cell in the stack [5]. The cooling plate may also have serpentine flow channel. For optimum performance, good distribution of the reactants throughout the stacks is necessary. It is also necessary to minimize the pressure drop in the flow of gases through the stack as pumping power reduces the overall efficiency of the system. Thus, good knowledge of the flow details in the serpentine channels of such stacks is necessary for optimum design.

The various flow configurations, shown schematically in Fig. 1 on a typical distributor plate, can be viewed as combinations of straight and bend sections of ducts of rectangular cross-section. Typically, the channel sizes and the gas flow rates are small and the flow is expected to be laminar. This poses special problems for the determination of the pressure losses because the loss coefficients in laminar flow depend strongly on the Reynolds number (*Re*). Examples of such

* Corresponding author. Tel.: +91 44 4458227; fax: +91 44 2350509.
E-mail address: sjayanti@iitm.ac.in (S. Jayanti).

0378-7753/$ – see front matter © 2004 Elsevier B.V. All rights reserved.
doi:10.1016/j.jpowsour.2004.06.025

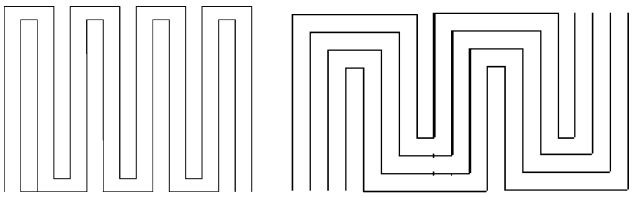

Fig. 1. Different flow fields of bipolar plates in planar fuel cells for: (a) single serpentine channel; (b) parallel serpentine channel.

Reynolds number dependence are the drag coefficients for flow over a sphere [6] and the discharge coefficient for flow through an orifice plate [7]. The channel aspect ratio also has to be taken into consideration as the use of the hydraulic diameter to evaluate the Reynolds number can lead to significant errors under laminar flow conditions [8]. Finally, there is extensive literature on turbulent flow through circular and non-circular ducts with bends.

Detailed measurements of the velocity field in bends of circular and square cross-sections of varying bend radius-to-duct diameter ratios have been reported by Humphrey et al. [9], among others. Data on loss coefficients are well documented for various curvature ratios (C) for curved pipes [10–13]. The use of guide vanes to improve the flow distribution through sharp bends has been studied experimentally by Ito and Imai [14] and computationally by Modi and Jayanti [15]. By contrast, the literature on laminar flow through bends is rather limited. There are relatively fewer studies of laminar flow through 90 and 180° bends. Humphrey et al. [16] used laser-doppler anemometry to study the laminar flow through a square curved duct with a Dean number of 368 and a curvature ratio of 4.6. These workers also conducted numerical studies on developing laminar flow in circular cross-sectioned bends. Miyaka et al. [17] reported numerical studies on curved ducts of rectangular cross-section and described the flow mechanism in the entrance and the exit resions. Measurements of the pressure drop for laminar flow through 90° bends of circular cross-section have been reported by Beck [18]. Correlations for bend loss resistances for various bend configurations have been discussed in detail by Idel'chik [13], but these are applicable only for $Re > 10000$. It was noted that the loss coefficient in the laminar regime would show a large variation but no guidelines were provided for its calculation.

Thus, detailed information of the laminar flow through the serpentine channels of fuel cells is not available in the literature. The present investigation is motivated by a need to provide an understanding of the flow in the channels of fuel cells and to develop design correlations for bend loss coefficients in the parametric range of interest to designers of fuel cell stacks. Given the small size of these channels, experimental studies are difficult. Taking advantage of the reliability of computational fluid dynamics (CFD) simulations for steady laminar flows (as will be demonstrated later), a systematic numerical study has been conducted to understand the flow structure and related phenomena in laminar flow through 90 and 180° bends over a range of curvature ratios and aspect ratios. The effect of upstream bend on the bend loss coefficient has also been systematically studied.

2. Methodology

2.1. Problem formulation

The present calculation methodology is based on CFD simulations in which the fundamental equations governing the flow, namely the conservation of mass and momentum for an incompressible isothermal flow are solved numerically. The governing equations are non-linear, second-order, coupled partial differential equations. Upon discretization either by finite difference, finite volume, finite element or other similar methods, each partial differential equation is converted into a set of non-linear algebraic equations. The unknowns are the values of the conserved variables associated with each grid or node. These algebraic equations are linear zed and are solved simultaneously using iterative methods to obtain the field values of the variables at the pre-specified grid locations. CFD techniques for fluid flow problems have become well developed (see for example [19,20]) and give reasonably accurate results for a range of single-phase flow problems. They have previously been applied to fuel-cell applications [2,21]. The present objective is to conduct a systematic study of laminar flow through typical gas distributor plates in fuel cells with the intention of developing design correlations. This has not been done previously. The governing equations, assuming incompressibility are:
mass balance equation:

$$\frac{\partial (U_i)}{\partial x_i} = 0 \tag{1}$$

momentum balance equation:

$$\frac{\partial (U_j U_i)}{\partial x_j} = -\frac{1}{\rho}\frac{\partial P}{\partial x_i} + \frac{\partial}{\partial x_i}\left(v\frac{\partial U_i}{\partial x_j}\right) \tag{2}$$

where $i = 1, 2, 3$.

Here, U_i is the component of velocity in the i-direction; P is the static pressure, ρ and v are the fluid density and kinematics viscosity, respectively.

In the present study, the CFX code (version 4.3), which is a commercially available, finite-volume, method-based CFD developed by AEA Technology, UK, is used for the calculations. It is a widely used code for a variety of flow situations and contains a number of application-specific models such as for turbulence, chemical reactions, combustion and radiation. These models introduce a degree of empiricism into the governing equations, the severity of which depends on the application and on the model chosen. In the present case of laminar flow through bent ducts, no such empiricism is introduced except that related to the assumption of incompressible, isothermal flow of a Newtonian fluid. These

assumptions should be valid for typical fuel-cell applications where the pressure drops are fairly low, the temperatures are fairly constant and the physical dimensions, though small, are sufficiently large for continuum hypothesis to be valid. The estimated Knudson number for air flow is around 0.00007, which is much less than unity. Also, the hydraulic diameter of the channel is of the order of 1 mm, and experiments [22,23] show that the flow remains laminar up to a *Re* of about 2100. Hence, special considerations associated with micro- or nano-scale phenomena [24] are not warranted in the present problem, Therefore, main source of error in the calculations arises from spatial discretization and finite convergence limits imposed on the solution of the discretized equations. These aspects are discussed later.

2.2. Details of the calculation scheme

The geometry studied in the present work consisted of 90 and 180° bend(s) in a duct of rectangular cross-section. Simulations were carried out for: (i) a square bend, i.e., with a curvature ratio C of R_c/D_h where R_c is the mean radius of the bend and D_h is the duct hydraulic diameter, i.e., $D_h = 4wh/2(w + h)$, where w and h are width and depth of the channel (ii) gradual bends. Typically, each bend was provided with a 100 diameter-long duct section upstream and a 100 diameter-long section downstream for flow development. Taking advantage of the symmetry, only one-half of the duct cross-section was simulated. Accordingly, the boundary conditions imposed were:

- normal velocity specified as the mean flow velocity at the upstream 'inlet';
- fully developed flow condition specified at the downstream 'outlet';
- no-slip condition (zero velocity for normal and tangential velocity components) on the side walls;
- symmetry condition (zero normal gradient) specified on the symmetry plane.

The nominal fluid properties corresponded to those of air at atmospheric conditions. The Reynolds number based on the mean velocity and the hydraulic diameter was varied between 0.7 and 2300.

The cross-section of the duct was discretized by using a structured mesh with 20 cells in the width direction and 12 cells in the half-depth direction. Since the location of the maximum velocity gradient changes location as the flow goes through the bend, a uniform mesh was employed in the cross-section of the duct. Along the axis of the duct, a non-uniform grid was employed to enable better resolution of the velocity gradients near the bend. A systematic study of grid independence was carried out, as discussed later, to verify that this grid is adequate. All the simulations were conducted by means of a segregated method using the SIMPLE scheme [19] for pressure-velocity decoupling. Nominally second order-accurate schemes were selected for the discretization of the governing equations. A residual reduction factor of 10^{-10} for the mass conservation equation was used to monitor the convergence of the iterative scheme.

A number of configurations were studied using the above methodology. A typical variation of the velocity (plotted in terms of contours of the magnitude of the velocity) in the symmetry plane in the region of the bend (*Re* of 706, sharp bend) is shown in Fig. 2(a).

There is significant distortion of the velocity field as the flow goes through the bend and a large recirculation bubble downstream of the bend can be clearly seen. The variation of the dimensionless static pressure drop (pressure drop/kinetic head) along the center-line of the duct and along the inner and the outer walls in the symmetry plane are shown in Fig. 2(b) As expected, the pressure variation is linear well away from the bend; within the bend, however, there is a significant variation in pressure. The flow undergoes favourable and adverse pressure gradients along the inner and outer walls, respectively, before the bend. The trend is reversed in the latter part of the bend; acceleration now occurs along the region near the outer wall, while deceleration takes place along the inner wall. These changes, if sufficiently strong, can lead to flow separation and the formation of recirculation bubbles near the outer wall in the initial part of the bend and near the wall in the latter half of the bend in turbulent flow [6,12]. In laminar flow, whether or not, flow separation occurs is a strong function of both the Reynolds number and the curvature ratio, as will be shown later.

Extrapolation of the linear sections of the pressure variation in the upstream and downstream sections of the duct shows that there is a net pressure drop as the flow goes through the bend. The definition of the bend pressure loss refers to such stations on either side of the bend where the static pressure is constant over the cross-section. The schematic of the pressure variation shown in Fig. 3(a) can be used to explain the definition of the bend pressure-loss coefficient. Here, ΔP_1 is the pressure loss in the straight pipe between points A and F in the absence of a bend. In the presence of a bend, ΔP_2 is the pressure loss that is added due to skin friction of the straightened length of the bend region. ΔP_3 is the pressure loss associated with wake friction due to the bend. Thus, the bend pressure loss includes both ΔP_2 and ΔP_3 and a pressure-loss coefficient (K_b) can be defined [12] as:

$$K_b = \frac{\Delta P_2 + \Delta P_3}{1/2\rho V^2} \tag{3}$$

where V is the mean velocity. The excess loss coefficient ξ, in which the pressure loss associated with skin friction, ΔP_2, is subtracted, can be defined as:

$$\xi = K_b - 4fC\theta \tag{4}$$

where: C is the curvature ratio, θ is bend angle in radian and is f the friction factor for fully developed straight duct flow. For a sharp bend there is no C, but the effective center-line of the length between the entrance and the exit of the bend can be taken ($C = 0$). Typical variations of the bend and excess loss coefficients with *Re* as calculated above are shown in

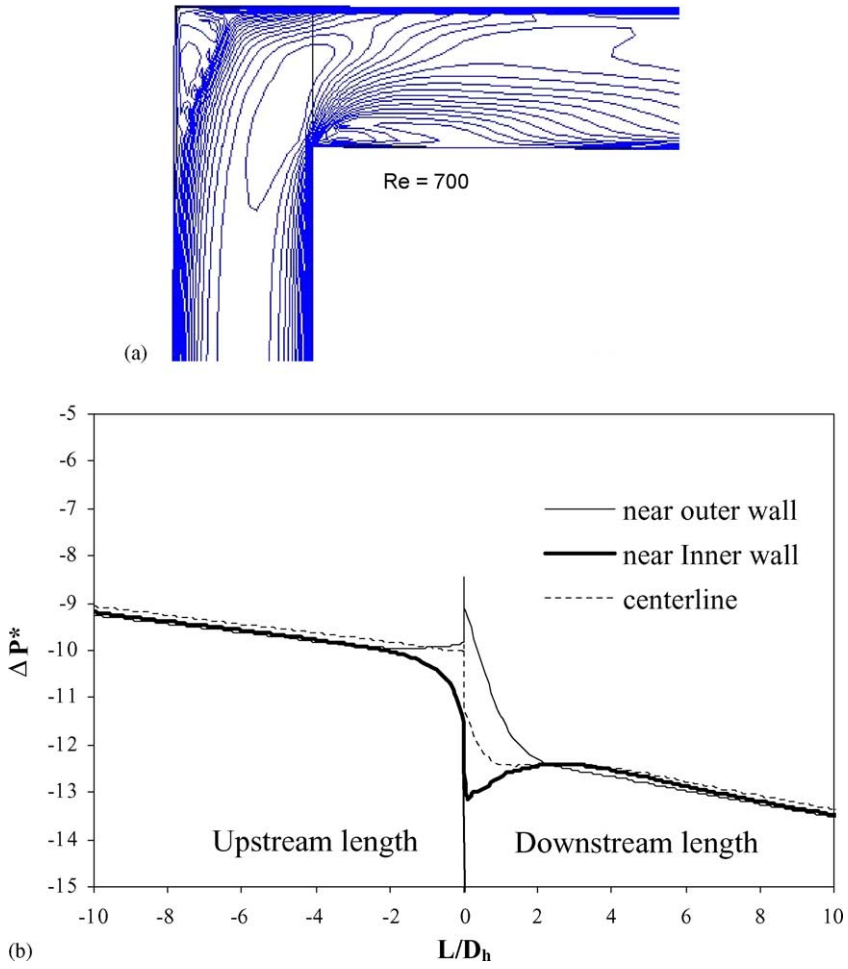

Fig. 2. (a) Velocity contour plot in symmetry plane for sharp bend at Reynolds number of 700. (b) Variation of dimensionless static pressure along center-line of duct and along inner and outer walls in symmetry plane for sharp bend.

Fig. 3(b) for particular bend geometry. The strong variation with Reynolds number is a significant feature of laminar flow through bends. The present objective is to determine this variation in terms of the significant parameters of the flow and to correlate the characteristics in such a way that the loss factor can be estimated using algebraic expressions without recourse to CFD simulation.

2.3. Validation

For laminar flow, the above calculation methodology does not introduce any empiricism in the fundamental equations. Accurate results can be obtained therefore if the solution method is sufficiently accurate. The principal source of error is due to discretization and convergence of the iterative scheme. To ensure the latter, both the residual factors for the individual balance equations and field values at a particular point within the flow domain have been monitored to obtain four significant digits in the field values. The discretization error depends on the grid density and to ensure grid independence of the results; calculations have been performed for a particular case of a sharp bend with a cross-sectional grid of 6×12, 10×12, 20×12, 40×12, 20×24, and 40×24. These show that the pressure drop obtained with a 20×12 grid is within 1% of that obtained with a 40×24 grid. The predicted axial velocity profiles in the downstream length of the bend with the two grids are also found to match well, which thus shows that the results obtained with a 20×12 are nearly grid-independent. Hence the 20×12 grid size is used for all the simulations. The computational grid of three-dimensional geometry consists of 240,000 cells with 20×12 grid size.

Further validation of the methodology is provided in Fig. 4 where the predicted parameters are compared with those obtained experimentally. In laminar flow, the friction factor in a straight duct varies inversely with Reynolds number, i.e., $f = C_s/Re$, where C_s is a constant of proportionality that depends on the shape of the cross-section. The predicted variation of this constant with the aspect ratio (width/height) of the rectangular duct is compared in Fig. 4(a) together with that predicted by the empirical correlations of Kays and Crawford [25] and Bhatti and Shah [26] over the range of $0.25 < a < 20$. Excellent agreement is obtained between the CFD predictions and the empirical correlations. Humphrey et al. [16]

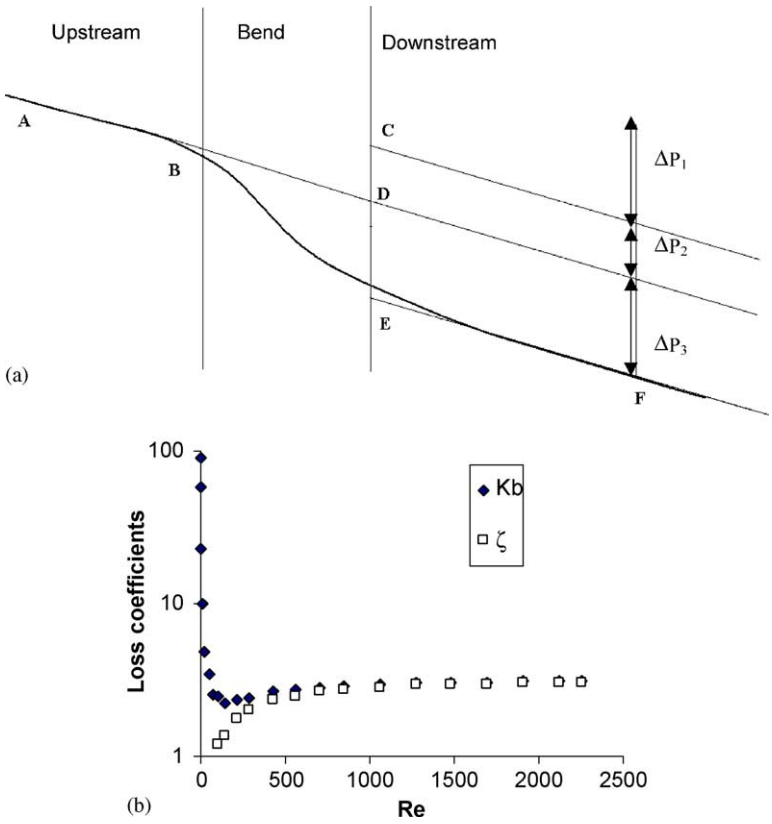

Fig. 3. (a) Schematic variation of center-line pressure in duct with bend (Ward-Smith, 1980) with identification of various pressure drop components. (b) Variation of bend and excess loss coefficients with *Re* for sharp bend.

measured the velocity field using laser-doppler anemometry in a 90° bend of square cross-section. The predicted axial velocity contours at the bend exit plane are compared with the measured values in Fig. 4(b) at a Reynolds number of 790. It can be seen that very good agreement is obtained between the two. Finally, the predicted bend loss coefficient for a 90° bend of rectangular cross-section is compared in Fig. 4(c) with the experimental data of Beck [18] for a bend of circular cross-section. Good agreement is obtained for both the curvature ratios over the entire range of Reynolds number.

The above comparisons show that accurate results of the flow field and the pressure loss can be obtained using the present calculation methodology. A number of cases have been studied to investigate the influence of various geometric parameters on the bend loss coefficients. The results are discussed below.

3. Results

3.1. Flow development

The development of the flow within the bend depends, under laminar flow conditions, principally on the Reynolds number curvature ratio and aspect ratio as well as on upstream effects such as the presence of an upstream bend. The effects of these are considered separately below.

3.1.1. Effect of Reynolds number

Contour plots of the velocity in the symmetry plane (z = 0) for a sharp 90° bend at different *Re*.are presented in Fig. 5. There is no flow separation for the flow with $Re < 50$, which is dominated by viscous forces, i.e., the skin friction would be much more when compared with the form friction. Separation at the inner corner appears at *Re* of 100, while significant recirculation at the outer corner appears at *Re* of about 200. The size and intensity of both vortices increase with increasing *Re*. At a Reynolds number of 706, the inner vortex occupies 20% of the width of the channel in the downstream of the bend. For *Re* 1000 and above, the shape and size of the inner recirculation bubble become almost constant.

The flow redevelopment length (L_r = downstream length/hydraulic diameter) downstream of the bend, i.e., the distance required for the flow to become fully developed, increases with Reynolds number. This is illustrated in Fig. 6(a) where the dimensionless axial velocity profiles downstream of the bend are shown at various distances for *Re* of 50, 141, 282 and 564. At low *Re*, the axial velocity profile is fully developed within 10 hydraulic diameters, whereas at *Re* of 564, a length of nearly 50 D_h is required for flow development. Since the distance between successive bends in a serpentine

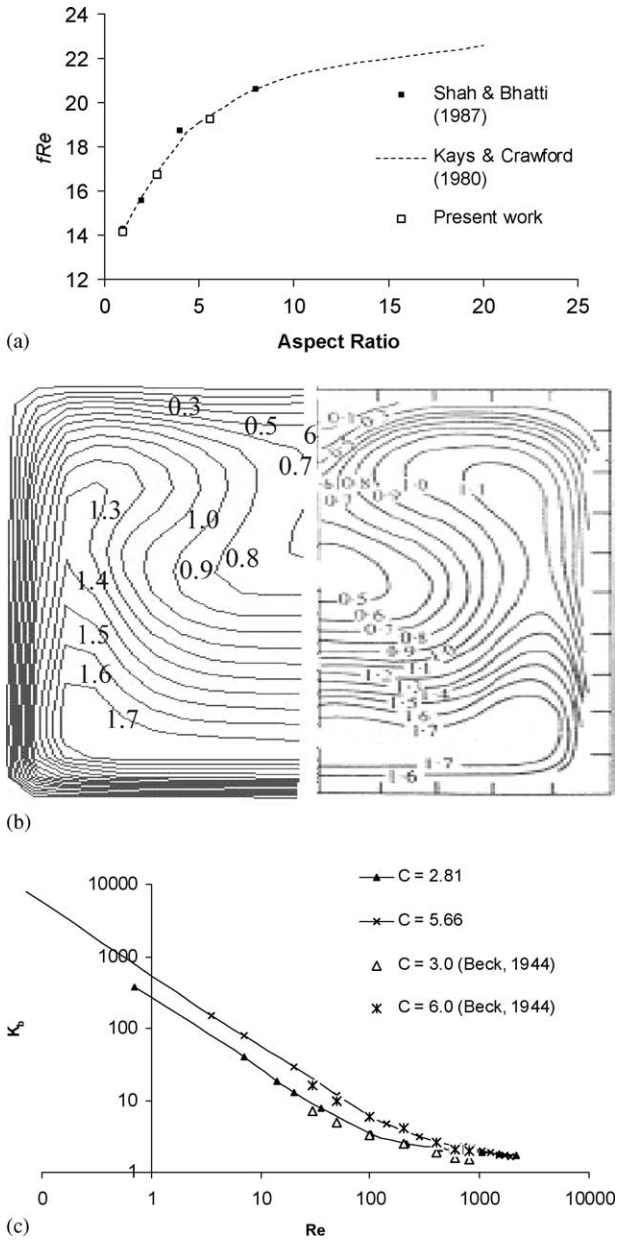

Fig. 4. (a) Comparison of predicted *fRe* with that of literature [25,26] for different aspect ratios. (b) Predicted axial velocity contours and measured values [16] at bend exit plane for *Re* = 790. (c) Comparison of bend loss coefficients with data of Beck [18].

channel configuration Fig. 1(b) is in the range of 5–25 D_h, the above results show that the flow field approaching the second bend is significantly distorted and may thus have a different bend loss coefficient, as will be shown later. The estimated flow re-establishment length, estimated from the present calculations, is plotted in Fig. 6(b) as a function of the Reynolds number. As expected [8], a nearly linear variation is obtained and the numerical data can be correlated as:

$$L_r = 0.1Re + 9 \quad (5)$$

3.1.2. Effect of curvature ratio

The onset and extent of significant flow separation depend on the curvature ratio *Re* defined as the ratio of the mean bend radius to the hydraulic diameter of the duct. For a gradual bend, i.e., for non-zero values of *Re*, no recirculation patterns are observed in the symmetry plane ($z = 0$) for all the *Re* and R_c/D_h ratios investigated. On the other hand, recirculation is observed at the outer wall near the *z* planes away from the symmetry plane at high *Re*. This is illustrated in Fig. 7 where the velocity contours in the plane close to the bottom wall are compared for different curvature ratios at the same Reynolds number. For a curvature ratio of 1.41, a recirculation zone near the outer wall is found for *Re* of 425. This outer wall recirculation zone is confined to between 0 and 20° into the bend. For a curvature ratio of 2.83, there are no recirculation zones throughout the bend as well as in the upstream and downstream sections. Some distortion in the flow near the outer wall of the bend can be observed at *Re* greater than 1500. At this *Re*, however, inception of a very small recirculation zone can be observed near the outer wall at around 5°. Similar results are obtained for a curvature ratio of 5.66. These results, obtained for an aspect ratio of 2.77, agree qualitatively with the experimental results reported by Humphrey et al. [16] for a curvature ratio of 2.5 in a duct of square cross-section. These authors observed small circulation zones near the outer wall between 0 and 25° and close to the top/bottom walls at *Re* of 790. Thus, the bend radius has a significant effect on whether or not flow separation occurs in the bend region; its effect on pressure loss coefficient is discussed later.

3.1.3. Effect of aspect ratio

As shown in Fig. 8(a), the present calculations for a square cross-section are in excellent agreement with the results of Humphrey et al. [16]. A square cross-section is not often used in fuel-cell applications however and therefore, the effect of a higher aspect ratio needs to be investigated. This is done by repeating the calculations for aspect ratios of 2.77 and 5.66. The results are summarized in Fig. 8(a) where the velocity profiles in the symmetry plane upstream and downstream of the bend are shown for different aspect ratios at *Re* of 100. These show typically that as the aspect ratio increases, the extent of flow distortion within the bend decreases. Thus, the effect of streamline curvature is less if the aspect ratio is more.

3.1.4. Effect of upstream bends

The effect of an upstream bend is illustrated in Fig. 8(b) where the velocity is presented for a case with two sharp bends separated by a short distance viz., 2- and 6-step hydraulic diameters, at a Reynolds number of 700. The close presence of an upstream bend suppresses the flow separation to some extent in the second bend. This beneficial effect is reduced as the bend separation distance increases.

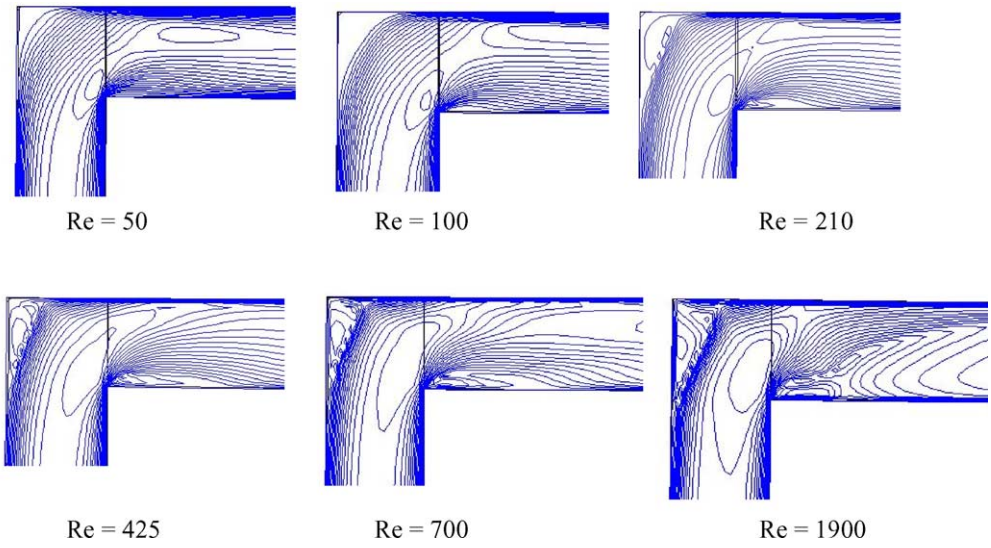

Fig. 5. Velocity contour plots at various Reynolds for sharp bend (a = 2.78) at different Reynolds number near bend.

3.2. Pressure loss coefficients

The bend loss coefficients were calculated by using Eqs. (3) and (4). Typical variations of the overall bend loss coefficient and the excess loss coefficient are shown in Fig. 9(a) as a function of the Reynolds number for three curvature ratios. It is seen that at very low *Re*, the loss coefficient is higher for a gradual bend than for a sharp bend. This is due to the fact that at these low *Re*, the pressure loss is governed by skin friction (as there is no flow separation) and this is higher in the gradual bend due to the longer overall length. At high *Re*, it is the losses resulting from flow separation that dominate the overall bend loss coefficient and the bend loss coefficient for a sharp bend is significantly higher than that for a smooth bend. When the skin friction component is deducted, a clearer picture of the loss coefficient value emerges as shown by the variation in the excess loss coefficient given in Fig. 9(b). It is found that the excess loss coefficient is always higher for a sharp bend even though it is negligibly small for $Re < 100$.

In addition to the curvature ratio and the Reynolds number, the excess loss coefficient depends on the aspect ratio and on the presence of an upstream bend, as expected from the discussion in Section 3.1 above. Examination of the results obtained from the present calculations (totalling about 190 individual cases) reveals the following:

- As the aspect ratio increases, the excess loss coefficient decreases. This is consistent with the observation above that as the aspect ratio increases, the intensity and extent of flow separation decreases.
- The effect of an upstream bend is beneficial in that the excess loss coefficient for two bends in series decreases as the distance between them decreases. This again is consistent with the flow pattern shown in Fig. 8(b) that demonstrates that a close upstream bend tends to suppress flow separation at the bend exit. Similar results have been reported by Modi and Jayanti (2004) for turbulent flow. These authors, however, noted that the effect is not always monotonic and that certain bend combinations may lead to an increase in the bend loss coefficient.

3.3. Correlation for the excess loss coefficient

Based on the above simulations, a three-regime correlation is developed for the excess bend loss coefficient as a function of the Reynolds number, aspect ratio (a), curvature ratio (C) and the distance between successive bends, if any. The three-regime correlations are based on the flow patterns and structure, which has been discussed earlier (Section 3.1). The division into three regimes is based on the Reynolds number: for $Re < 100$, the excess loss coefficient is zero; for $Re > 1000$, it is independent of *Re*; for intermediate *Re*, it is a strong function of *Re*. The proposed correlations are as follows:

For $Re < 100$:

$$\xi = 0 \tag{6a}$$

For $100 < Re < 1000$:

$$\xi = 0.46\,(Re^{1/3})\,(1 - 0.18C + 0.016C^2) \times (1 - 0.2a + 0.0022a^2) \times \left(1 + 0.26\left(\frac{L_s}{D_h}\right)^{2/3} - 0.0018\left(\frac{L_s}{D_h}\right)^{2}\right) \tag{6b}$$

For $1000 < Re < 2200$:

$$\xi = 3.8\,(1 - 0.22C + 0.022C^2)\,(1 - 0.1a + 0.0063a^2) \times \left(1 + 0.12\left(\frac{L_s}{D_h}\right)^{2/3} - 0.0003\left(\frac{L_s}{D_h}\right)^{2}\right) \tag{6c}$$

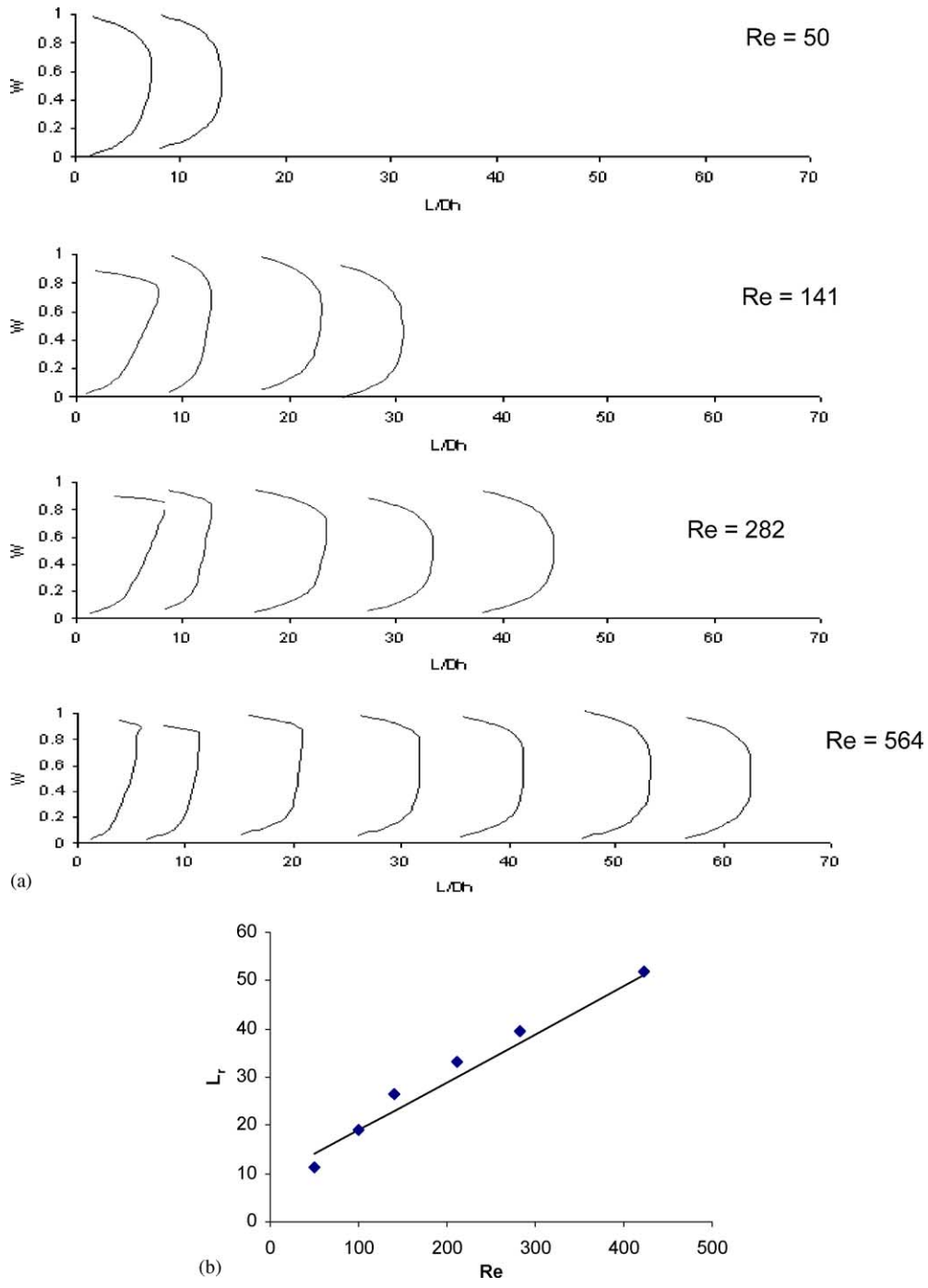

Fig. 6. (a) Velocity profiles along the downstream length of the sharp bend (a = 2.78) at Reynolds number of 50, 141, 282 and 564. (b) Variation of dimensionless flow redevelopment length with Reynolds number after bend for sharp bend (a = 2.78).

The correlations given by Eqs. (6(a–c)) are valid for the following range of parameters:

$0 < Re < 2200$

$1 < a < 6$

$0 < C < 6$

$$1 < \frac{L_s}{D_h} < 30$$

It should be noted that the aspect ratio here is defined as the width divided by the depth of channel, where the width is in the plane of the bend, while the depth is in the direction parallel to the bend axis. When compared with the CFD-generated data, the above correlations

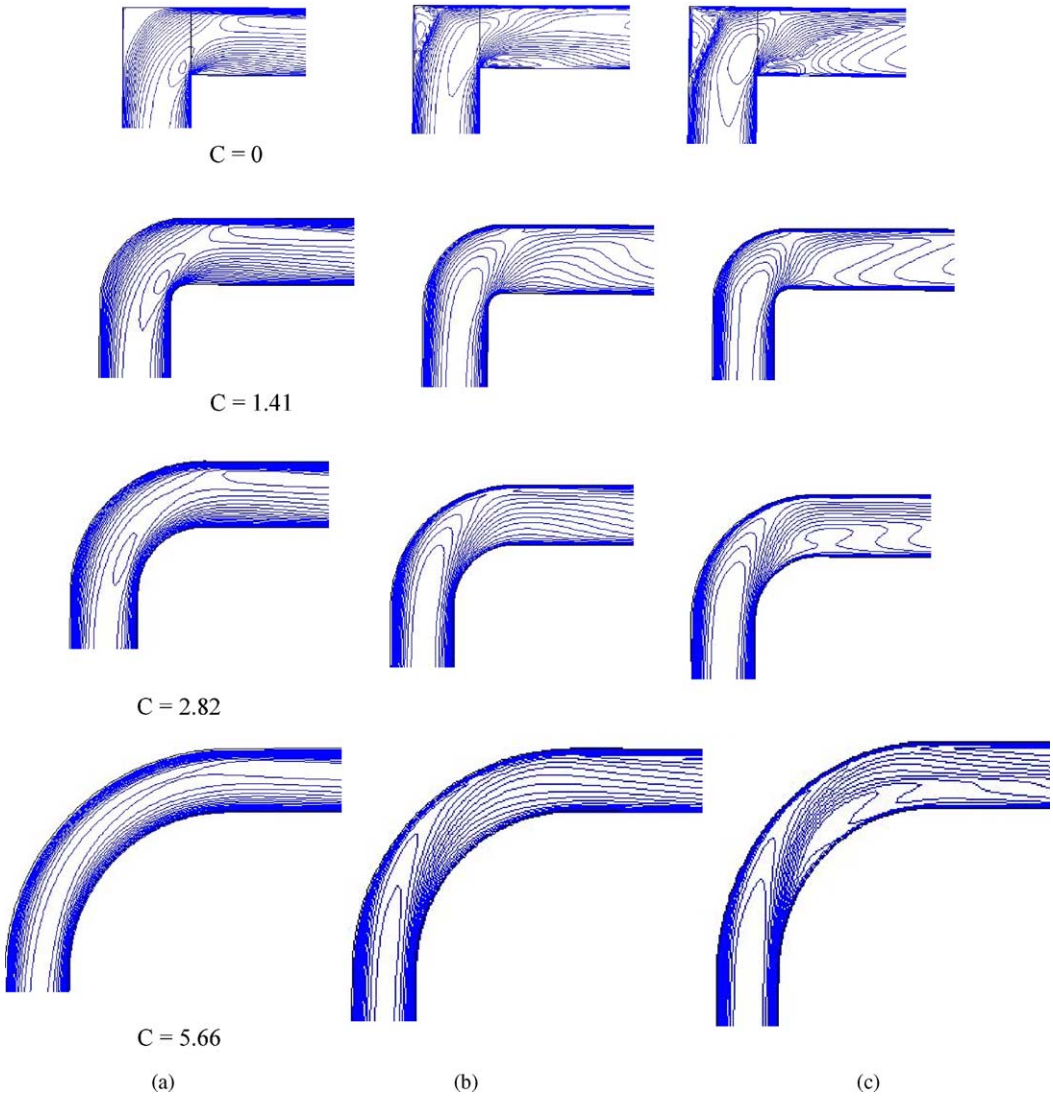

Fig. 7. Velocity contour plots for different curvature ratios (C) at Reynolds numbers: (a) 100 (b) 700 and (c) 2100 near the wall plane.

predict an excess loss coefficient with a standard deviation of about 6%.

4. Application to fuel cell stacks

The above set of results and correlations can be used in a typical fuel cell application. Consider for example, the case of a serpentine configuration of fuel cell with sharp bends. The serpentine channel consists of straight sections that are connected in the corners where the flow is redirected, as can be seen in Fig. 1. Neglecting entrance and exit losses (that are expected to be small in comparison with the overall pressure drop), the total pressure drop between the inlet and the outlet of the bipolar plate on the cathode or anode side can be decomposed into two components, namely the pressure drop due to straight pipe friction and that due to the bends. As mentioned above, the latter is calculated in terms of an excess loss coefficient defined by Eq. (4), while the straight pipe friction within the bend is to be accounted for separately. Thus, the total pressure drop is given by:

$$\Delta P_{\text{tot}} = \frac{1}{2}\rho V^2 \left(K_f^* + \sum_{i=1}^{n} \xi_i \right) \tag{7}$$

where K_f^* includes the frictional loss suffered in the elongated section of the bends, and the second term constitutes the sum of excess loss coefficients for n U-bends in the serpentine channels. For parallel serpentine channels, the above equation is applied by assuming, uniform flow distribution through each channel. The straight pipe frictional resistance coefficient is given by:

$$K_f^* = 4f \frac{L_{\text{t}}}{D_{\text{h}}} \tag{8}$$

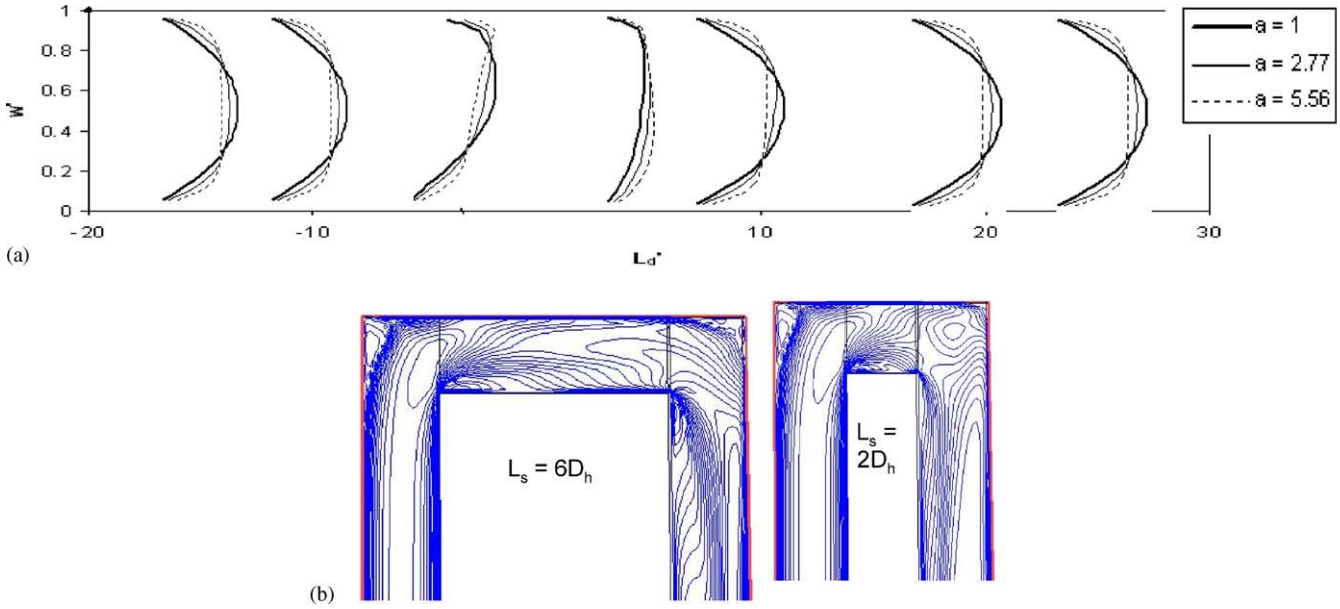

Fig. 8. (a) Velocity profiles in symmetry plane upstream and downstream of bend for different aspect ratios at *Re* of 100. (b) Velocity contour plots for different spacer lengths at a Reynolds number of 700 in symmetry plane of 180° bends.

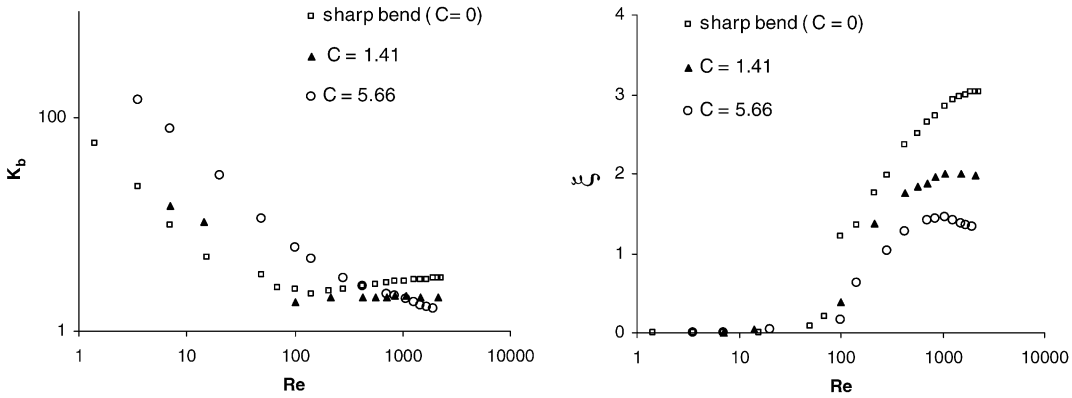

Fig. 9. Variation of (a) bend loss coefficient and (b) excess bend loss coefficient of gradual bends with Reynolds number.

where L_t is the total length including the length (based on mean radius of curvature of the bend) in the bends and/is the friction factor given, for example, by the empirical correlation of Kays and Crawford [25]:

$$Ref = 13.84 + 10.38 \exp\left(\frac{-3.4}{a}\right) \quad (9)$$

By way of illustration, pressure drop calculations for a short serpentine channel, single serpentine channels and parallel serpentine channels for different aspect ratios in distributor plates are discussed below.

4.1. Short serpentine channel

Consider the case of a serpentine channel with a total length of 250 mm and containing five straight channels of 50 mm length connected by four 180° bends. The pressure drops over a range of mass flow rates are calculated using the above set of correlations and are compared in Table 1 with those obtained by a direct simulation using the CFX computer code. Excellent agreement between the two sets of data is obtained. This result shows that the approach outlined above can be used to calculate the pressure drop for a given configuration, and can thus be used to optimize the design.

Table 1
Comparison of pressure drop calculated directly from CFD simulations and from developed correlations for short serpentine channel

Re	ΔP (Pa)	
	Direct simulations	Correlations
100	2.03E+02	2.00E+02
212	4.73E+02	4.57E+02
424	1.10E+03	1.07E+03
706	2.13E+03	2.19E+03

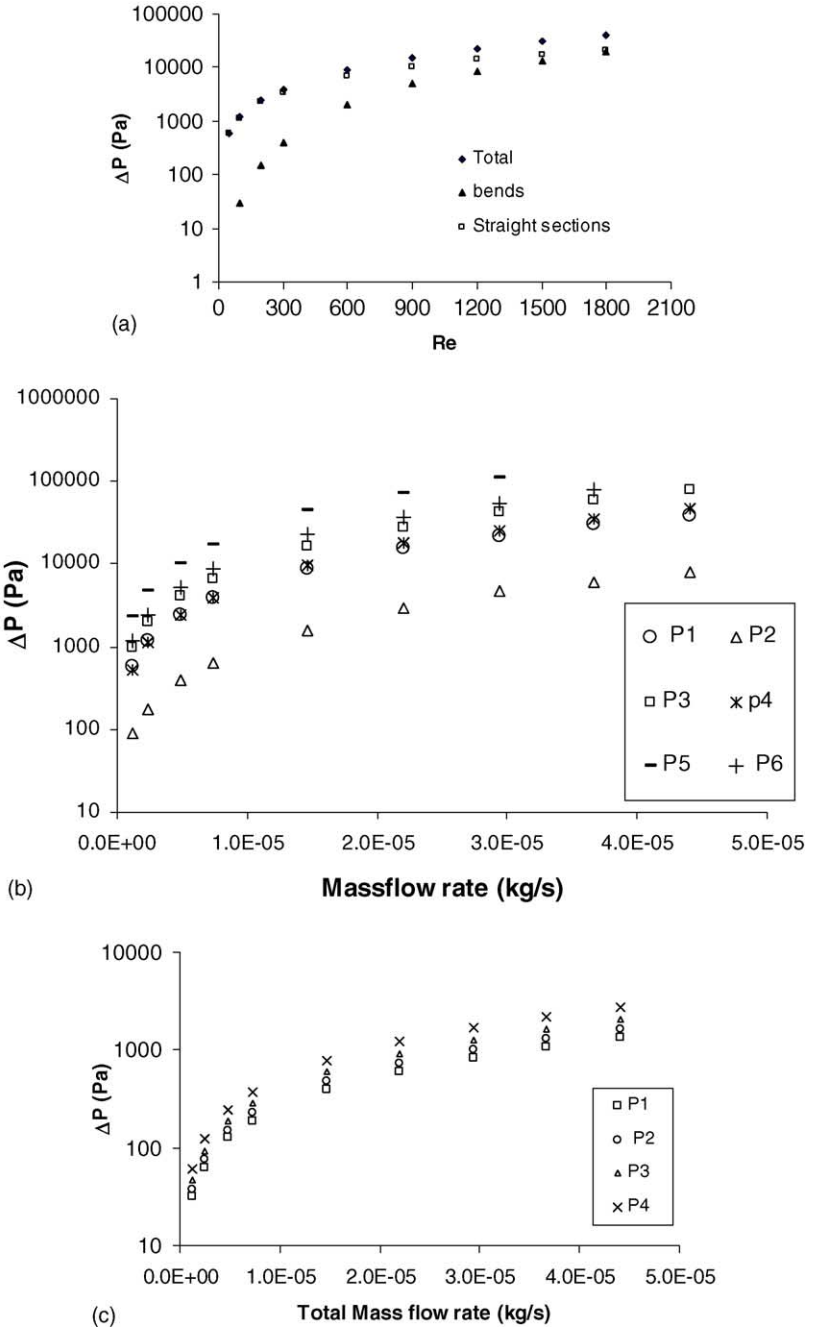

Fig. 10. (a) Variation of total pressure drop and its components with Reynolds number for single serpentine channel. (b) Pressure drop for various aspect ratios of single serpentine chancel, parameter indicated in parentheses are ($w \times h$, D_h (mm)): $P1$ = (2 × 0.72, 1.06); $P2$ =(2 × 1.5, 1.7); $P3$ = (1.5 × 0.72, 0.98); $P4$ = (1.5 × 1.1, 1.2); $P5$ = (1 × 0.72, 0.84); and $P6$ = (1 × 1, 1). (c) Pressure drop for various parallel serpentine channels. Parameters indicated in parentheses are ($w \times h$, D_h (mm): $P1$ = four parallel channels (2.75 × 0.72, 1.141); $P2$ = five parallel channels (2 × 0.72, 1.06); $P3$ = six parallel channels (1.5 × 0.72, 0.98); $P4$ = seven parallel channels (1.14 × 0.72, 0.88).

This is illustrated below with an example, which also identifies the principal contributors to the pressure drop in a fuel cell stack.

4.2. Single serpentine channel–effect of aspect ratio

The Pressure drop has been calculated for a fuel-cell distributor plate with an active area of 60 cm^2 (100 mm × 60 mm). The reference case is that of a single serpentine channel with sharp bends and a channel width of 2 mm, a depth of 0.72 mm and rib width of 2 mm between channels. The straight pipe friction component and the bend loss component for this configuration are shown in Fig. 10(a) for a range of Reynolds numbers. In order to facilitate comparison at low *Re*, the pressure drop is plotted on a logarithmic scale. It can be seen that for $Re < 1000$, the bend component of pressure

drop is significantly less (by a factor of two or more) than the straight pipe friction. At higher Reynolds numbers, however, it is nearly as much as the straight pipe component. The effect of changing the dimensions of the channel (width and depth), which will exert an influence on the hydraulic diameter and thus on the straight pipe friction component, is shown in Fig. 10(b) Since both the mean velocity and the hydraulic diameter are changed in this process, it is no longer possible to compare the results on a Reynolds number basis, and the pressure drop for a given mass flow rate (of air) are compared here. The reference case with a width × depth × hydraulic diameter of 2 mm × 0.72 mm × 1.058 mm is shown as a solid line, while the geometric parameters corresponding to other combinations are marked in the legend. It can be seen that decreasing the channel width while keeping the depth constant decreases the hydraulic diameter and leads to a large increase in the pressure drop. By contrast, increasing the depth while keeping the width constant increases the hydraulic diameter and the pressure drop decreases by a large factor. In the case of a 1.5 × 1 × 1.2-system, an increase in hydraulic diameter increases the pressure drop when compared to the reference case at higher mass flow rates while there is virtually no effect at low *Re*. This must be attributed to the higher bend losses that resulting from the higher mass flow rate due to the decreased cross-section, which nullifies the beneficial effect of increased hydraulic diameter. The effect of decreasing the rib width is to increase the overall length of the single serpentine channel and this increases simultaneously both the pressure drop and the active area.

4.3. Parallel serpentine channels–effect of number of channels

One way of decreasing the pressure drop in a distributor plate is to have parallel serpentine channels instead of a single serpentine channel. This has the effect of reducing the flow rate through each channel, which decreases the pressure drop. At low *Re*, the pressure drop variation with the number of parallel channels will be linear. A more than linear variation may be expected at high *Re* because the bend losses, which are proportional to the square of velocity at high *Re* decrease more dramatically than the straight pipe friction component. This situation is illustrated in Fig. 10(c), in which the ribwidth is assumed to be 1 mm. It can be seen that the use of five parallel channels in a serpentine configuration with five turns, instead of a single channel (with about 20 turns) with the same cross-section, decreases the pressure drop by an order of magnitude. The effect of changing the width and depth of the parallel channel serpentine configuration is also shown in Fig. 10(c). If the channel's width is reduced, it is assumed that extra parallel channels are added as a means of compensation, while an increased channel width is accommodated by reducing the number of parallel channels. Thus, the length of each serpentine configuration is roughly the same. Under these conditions (other configurations are possible), the data in Fig. 10(c) shows that the pressure drops for different combinations can vary by a factor of two. The active area of the distributor plate, that is the area of fluid exposed to the porous electrode, also varies by about 25%. Calculations of this type can be combined with other criteria such as high pressure drop that is required to prevent flooding of the electrodes [27,28] and low pressure drop that is required to reduce pumping costs, and the rib width/active area considerations can be used to optimize the distributor plate configuration.

5. Conclusions

The pressure losses in a fuel cell stack are one of the important factors for overall fuel cell efficiency. The pressure drop in a fuel cell distributor plate depends on the plate configurations, and for a given serpentine channel configuration, it depends on geometric factors such as channel hydraulic diameter and bend geometry.

CFD-based simulations have been conducted for 90° bends with different curvature ratios (*C*) and different aspect ratios (*a*). The effect of successive bends for various spacer lengths (L_s 2–30 Dh) for full range of Reynolds numbers under laminar flow regime has been examined. The calculations show that there is a significant effect of *Re* on the bend loss coefficient, which is also influenced by the curvature ratio and the aspect ratio as well as the presence of an upstream bend. A correlation has been developed to predict the bend loss coefficient as a function of these parameters. Application of this correlation to typical fuel cell configurations shows that the bend losses constitute a significant portion of the overall pressure loss for $Re > 1000$. Considerable scope exists for the optimization of the channel configuration (in terms of width, height and gap) to achieve a desired pressure drop and keeping in view the need to reduce pumping costs while maintaining a sufficiently high pressure drop to avoid flooding of the channels. The results from this work will be very useful for such an optimization.

Acknowledgements

The work reported here has been carried out under a research grant from the Ministry of Non-conventional Energy Resources, India. The CFD computations have been carried out using the facilities of the CFD Center, IIT-Madras, India.

References

[1] H. Dohle, A.A. Kournyshev, A.A. Kulikovsky, J. Mergel, D. Stolen, Electrochem. Commun. 3 (2001) 73–80.
[2] V. Garau, L. Hongtan, S. Kakac, AIChE J. 44 (1998) 2410–2422.
[3] T.V. Nguyen, J. Electrochem. Soc. 143 (1996) L103–L105.
[4] P.W. Li, L. Schaefer, Q. Wang, Zhang M.K. Chyu, J. Power Sources 113 (2003) 90–100.

[5] E. Middelman, W. Kout, B. Vogelaar, J. Lenssen, E. De wall, J. Power Sources 118 (2003) 44–46.
[6] H. Schlichting, Boundary-Layer Theory, 6th ed., McGraw Hill, New York, 1968.
[7] W.H. Perry, Chemical Engineer's Handbook, 6th ed., McGraw Hill, New York, 1984.
[8] F.M. White, Viscous fluid flow, 2nd ed., McGraw-Hill, Inc, New York, 1991.
[9] J.A.C. Humphrey, J.H. Whitelaw, G. Yee, J. Fluid Mech. 103 (1981) 443–463.
[10] H. Ito, J. Basic Eng. Trans. ASME (1960) 131–142.
[11] D.R. Blevins, Applied Fluid Dynamics Handbook, Van Nostrand Reinhold Co Inc, New York, 1984.
[12] A.J. Ward-Smith, Internal Fluid Flow, Oxford University Press, New York, 1980.
[13] I.E. Idel'chik, Handbook of Hydraulic Resistances, 3rd ed., Jaico Publishing House, Mumbai, 1986.
[14] H. Ito, K. Imai, J. Basic Eng. Trans. ASME D (1966) 684–685.
[15] M. Modi, S. Jayanti, Trans. IChem E, Chem. Eng. Res. Des. 82 (2004) 321–331.
[16] J.A.C. Humphrey, A.M.K. Taylor, J.H. Whitelaw, J. Fluid Mech. 83 (1977) 509–527.
[17] Y.Miyaka, T. Kazishima, T.Inaba, International Conference on Experimental Heat Transfer, Fluid Mechanics and Thermodynamics, 1988.
[18] C. Beck, J. Am. Soc. Naval Eng. 56 (3) (1944) 366–388.
[19] S.V. Patankar, Numerical Heat Transfer and Fluid Flow, Hemisphere, Washington, DC, 1980.
[20] J.H. Ferziger, M. Peric, Computational Methods for Fluid Dynamics, Springer, Berlin, Germany, 1980.
[21] A. Kumar, G.R. Reddy, J. Power Sources 113 (2002) 11–18.
[22] T.S. Zhao, Q.C. Bi, Int. J. Heat Mass Transfer 44 (2001) 2523–2534.
[23] B. Agostini, B. Watel, A. Bontemps, B. Thonon, Exp. Therm. Fluid Sci. 28 (2004) 97–103.
[24] M. Gad El-Hak, J. Fluids Eng. Trans. ASME 121 (1999) 1–29.
[25] W.M. Kays, M.E. Crawford, Convective Heat and Mass Transfer, McGraw-Hill, New York, 1980.
[26] M.S. Bhatti, R.K. Shah, in: S. Kakak, R.K. Shah, W. Aung (Eds.), Handbook of Single-phase Convective Heat Transfer, Wiley, New York, 1987.
[27] J.J. Baschuk, X. Li, J. Power Sources 86 (2000) 181–195.
[28] T. Klaus, P. David, C. Hebling, J. Power Sources 124 (2003) 403–414.